Eur. Phys. J. D (2019) 73: 252
https://doi.org/10.1140/epjd/e2019-100466-y

THE EUROPEAN PHYSICAL JOURNAL D

Regular Article

Interaction of photoionisation and meteoric input in the atmosphere of Jupiter*

Laurence Campbell[1,a], Darryl B. Jones[1], Ronald D. White[2], Gustavo García[3], Oddur Ingólfsson[4], M. Cristina A. Lopes[5], and Michael J. Brunger[1]

[1] College of Science and Engineering, Flinders University, G.P.O. Box 2100, Adelaide, SA 5001, Australia
[2] College of Science and Engineering, James Cook University, Townsville, Queensland 4810, Australia
[3] Instituto de Física Fundamental, CSIC, Serrano 113-bis, 28006 Madrid, Spain
[4] Science Institute, University of Iceland, Dunhaga 3, IS-107 Reykjavik, Iceland
[5] Departamento de Física, Universidade Federal de Juiz de Fora, Juiz de Fora, MG 36936-900, Brazil

Received 24 September 2019 / Received in final form 23 October 2019
Published online 10 December 2019

Abstract. Interplanetary dust grains and meteoroids are assumed to deliver oxygen to the atmosphere of Jupiter. A current photochemical model overestimates the resultant density of water relative to an available measurement. This paper investigates whether the interaction of photoionisation and meteoric products can explain that discrepancy. As any process that breaks up water molecules is likely to produce hydroxyl, the predicted densities of hydroxyl are also investigated as a possible target for remote sensing. It is found that the densities of water are not changed by the addition of photoionisation, but that higher OH densities are predicted above about 400 km.

1 Introduction

The atmosphere of Jupiter is composed of H_2, He, H and CH_4, with oxygen assumed to be added by interplanetary dust grains and meteoroids (hereafter referred to collectively as meteoroids) containing CO, H_2O and CO_2. Moses et al. [1] introduced a photochemical model in which photodissociation of these molecules and subsequent chemical reactions leads to many oxygen bearing compounds. However, if the meteoroids are assumed to be composed of water ice, the model predicts an abundance of H_2O that is much higher than an available measurement [2].

Campbell and Brunger [3] emulated the model of Moses et al. and then used it to investigate whether dissociation, ionisation and reactions with meteor trails could explain the discrepancy. While the result was that the water densities were unchanged at the height of the measurement, densities of OH at upper altitudes were seen to be highly dependent on the processes involved. They raised the possibility that if electron-impact excitation cross sections for OH can be measured [4], then emissions from OH might be used for remote sensing of the processes by which oxygen is added to Jupiter's atmosphere. In the absence of measurements some theoretical values are available [5–7].

In the models above, photoionisation by sunlight was not considered. Such ionisation was modelled by Kim and colleagues [8,9]. In this current work the model of Moses et al. is modified to incorporate the photoionisation model of Kim et al., to investigate whether the inclusion of photoionisation can explain the discrepancy in the water densities and to predict the change in OH densities produced in reactions initiated by photoionisation.

The approach here is restricted to emulating the two previous models of Moses and Poppe [2] and Kim et al. [9] and combining them to provide a base for the current investigation that is established in the literature. Thus many other phenomena, such as the effects of dust, SO_2 input, aurora, the electron temperature distribution and electron-neutral processes, are not included. These possible complicating processes are considered in the discussion of the results.

2 Model description

The model is based on one described by Moses et al. [1], using rates of meteoroid input given by Moses and Poppe [2]. Photoionisation rates are calculated in an emulation of the model of Kim and Fox [8], with the subsequent ionic reactions taken from the assemblages of Kim and colleagues [8,9]. Some reactions with unspecified

* Contribution to the Topical Issue "Low-Energy Positron and Positronium Physics and Electron-Molecule Collisions and Swarms (POSMOL 2019)", edited by Michael Brunger, David Cassidy, Saša Dujko, Dragana Marić, Joan Marler, James Sullivan, Juraj Fedor.

[a] e-mail: laurence.campbell@flinders.edu.au

products are replaced with equivalent reactions from the Kinetic Database for Astrochemistry (KIDA) [10]. The simulation of the atmospheric densities resulting from the mix of reactions was performed by an implicit time-step calculation, as described by Campbell and Brunger [3].

2.1 Photochemical model

Altitude profiles of the densities of H_2, He and H, pressure, temperature, photodissociation rate constants and eddy diffusion coefficients were taken from supplementary data of Moses et al. [1]. Methane densities were calculated by application of molecular diffusion [11] to the value given by Moses et al. at the lower boundary (at −60 km). Gas input rates from meteoroid ablation were obtained from Figure 4 of Moses and Poppe [2].

Moses et al. [1] defined sets of chemical reactions (with rate constants) between the species produced by photodissociation of H_2, CH_4 and H_2O (including photodissociation of the products). This work uses their set of 120 photodissociation reactions and 232 chemical reactions in their "Model A". This photochemical model, together with vertical movement by molecular and eddy diffusion, was implemented in an implicit time-step calculation as described by Campbell and Brunger [3]. In this the products are calculated for each reaction and vertical diffusion flux for a time interval Δt and the densities of all species updated accordingly. As the densities approach equilibrium the values of Δt are increased, so the calculation can start with very small times steps (e.g. 10^{-8} s) and then adaptively increase the time step so that the simulation can run to equilibrium after about a thousand Earth years.

A subset of the chemical processes within the model is illustrated in Figure 1, which shows the transitions between oxygen-containing species at altitude 629 km. Each transition is represented by a vertical line drawn from the reactant (labelled symbol) to the product, positioned at the rate of the reaction (s^{-1}) on the horizontal axis. The density of each species is also shown by a horizontal line on the vertical axis. The meteoric input of water is represented by a larger circle.

In Figure 2 curves show the mixing ratios (fractions of total atmospheric density) as a function of pressure/altitude for H_2O, CO and CO_2 as calculated by Moses and Poppe [2] (from their Fig. 8) for the case where all the icy component is released as water. Error bars show the available measurements plotted in that figure. As described earlier, the measured value for water at about 100 km is significantly less than the calculated value.

The current model was initially run to determine a background atmosphere of hydrocarbons produced by photodissociation of H_2 and CH_4 and subsequent chemical reactions. Meteroid input, assumed to be all H_2O, was then added. The simulation was then run until the downward oxygen flux at the lower boundary was almost equal to that in the meteorid input, which occurred after about 1300 Earth years. The calculated mixing ratios of H_2O, CO and CO_2 are shown by symbols in Figure 2.

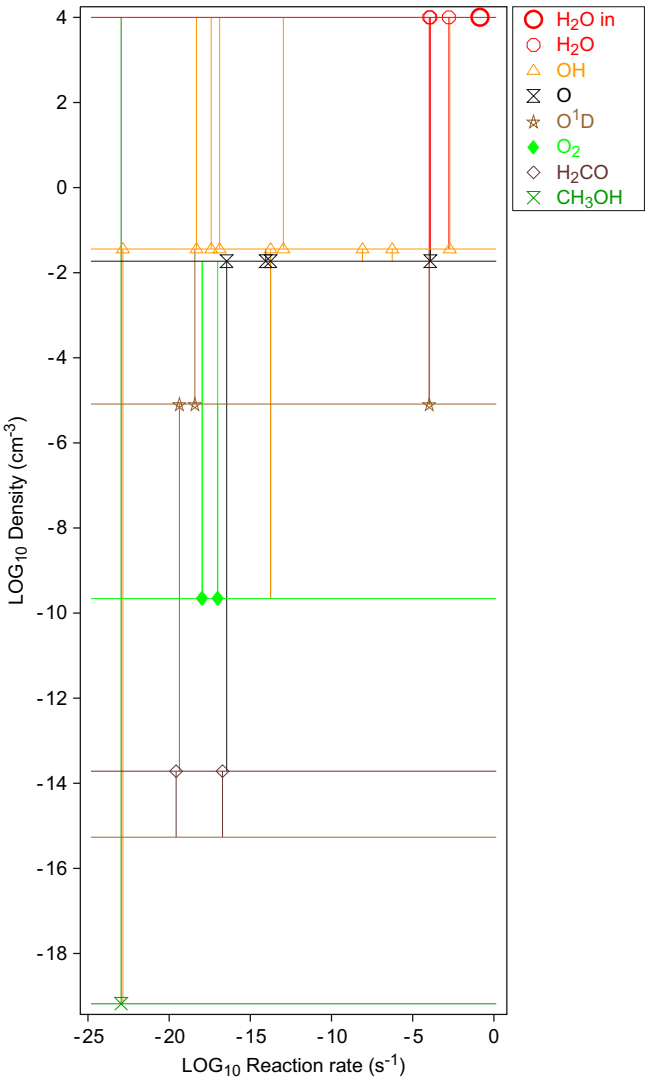

Fig. 1. Transitions between oxygen-containing species at 629 km, represented by lines joining reactants and products plotted at the reaction rate (s^{-1}) on the horizontal axis, with the densities of the species shown on the vertical axis. Reactants are identified by symbols described in the legend. The meteoric input rate of H_2O ("H_2O in") is shown by a larger circle.

Above about 110 km the agreement between the current implementation and that of Moses and Poppe ranges from fair for CO and CO_2 to very good for H_2O. In the range 0–110 km there is no agreement because Moses and Poppe apply a condensation model that was not implemented here. Below 0 km there is good agreement for H_2O, while the difference for CO is probably due to differences in the implementation of a lower boundary. Moses and Poppe set a fixed CO density at the lower boundary, which works in their equilibrium model but is not possible in the current time-step calculation because CO densities above the boundary would increase indefinitely. Instead the current implementation allows free flow through the lower boundary.

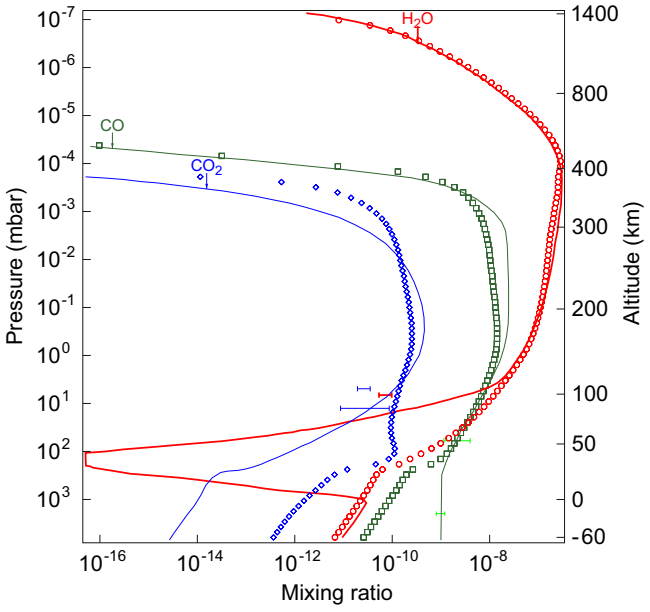

Fig. 2. Mixing ratios (horizontal axis) of H_2O, CO and CO_2 as a function of pressure (mbar)/altitude (km). Values calculated by Moses and Poppe [2] are shown by labelled curves. Error bars show measured values. Mixing ratios determined in the current implementation of that model are shown by symbols: H_2O (○), CO (□) and CO_2 (◇).

Despite the differences, the current implementation is shown in Figure 2 to agree with that of Moses and Poppe above 100 km to the extent that it can be used in further calculations to investigate the discrepancy between the measured and calculated water densities at 100 km.

2.2 Photoionisation model

Photoionisation rates were calculated by iteration over a series of height ranges where the absorption of solar radiation is calculated for each range and the solar insolation is reduced accordingly for input to the next height range below. This calculation requires a model of the short-wavelength solar spectrum and cross sections for photoabsorption by the atmospheric species present. The calculated flux at each successively lower height is then multiplied by photoionisation cross sections and the densities at that height (integrating over all wavelengths) to determine production rates of photoions.

To verify this model, its predictions of photoionisation rates were compared with values of Kim et al. [9]. To make this comparison, it was necessary to emulate the solar spectrum model used by Kim et al. This was stated to be the F79050 model of Hinteregger, referenced as a private communication and also a publication [12] in which most of the spectrum is integrated into 50-Å blocks. Kim and Fox refer to using this spectrum in a high resolution computation, implying that the spectrum given in private communication was a line spectrum. This inference is supported by a plot of a line spectrum in Figure 1 of Solomon et al. [13]. This line spectrum could not be found in literature or on the Internet. This work therefore used the similar "f76ref" spectrum [14], also measured by Hinteregger et al. [15] for the wavelength range 854–1116Å, scaled to have the same total flux as the low-resolution F79050 spectrum for that range. The spectrum thus derived is shown in Figure 3.

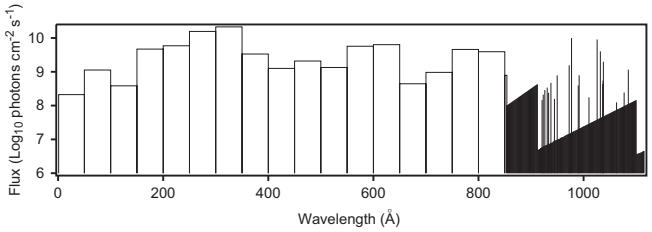

Fig. 3. The F79050 [12] solar spectrum, with the 854–1116-Å range replaced by a scaled section of the f76ref [14] spectrum.

Table 1. Source of photoabsorption cross sections.

Species	Source	Details
H	NIFS data base [16]	
H_2	Samson and Haddad [17]	
He	Kirby et al. [18]	
CH_4	Samson et al. [19]	Table II in reference

The absorption cross sections used are shown in Table 1 and the photoionisation cross sections in Table 2. Kim and Fox [8] found that by using a high-resolution photoabsorption spectrum for H_2 in the range 842–1116 Å, photons in the wings of the H_2 absorption lines can penetrate down to produce a layer of hydrocarbon ions. It was found here that, by omitting absorption in this region completely for H_2 and instead scaling the calculated H_2^+ production rate down by 25%, good agreement with the calculated values of Kim et al. was obtained. The comparison of this implementation with photoion production rates calculated by Kim et al. [9] is shown in Figure 4, indicating satisfactory agreement for the purpose of this study.

2.3 Combined model

To combine the models, the production rates of photoions are calculated for the initial atmosphere and then added as an extra reaction in the photochemical model. The values need to be updated as the densities of constituents change. As this is not computationally practical at every time step, the method was to run for a number of time steps (typically 10 000), then one would recalculate the ion production rates for the changed atmosphere before resuming the simulation.

To simulate the reactions of the added ions, the relevant ionic reactions of Kim and colleagues were added. These are all the reactions listed by Kim and Fox [8] (except R16) and the "Reactions involving O" in Table II of Kim et al. [9]. Several of these reactions (RC29, RC30, R101 and R108 of Kim and Fox and "$C_nH_nO^+ + e^- \rightarrow$ products" of Kim et al.) involved undefined products. For

Table 2. Sources of relevant ionisation cross sections for this study.

Molecule	Ion	Reference	Details
H	H^+	Samson [20]	Correction applied
CH_4	CH_4^+ CH_3^+, CH_2^+, CH^+ and C^+	Samson et al. [19]	
C_2H_2	$C_2H_2^+$	Hayaishi et al. [21]	Figure 2 in reference
H_2	H_2^+, H^+	Kossman et al. [22]	H_2^+, H^+ ratio from Backx et al. [23]
He	He^+	Kirby et al. [18]	

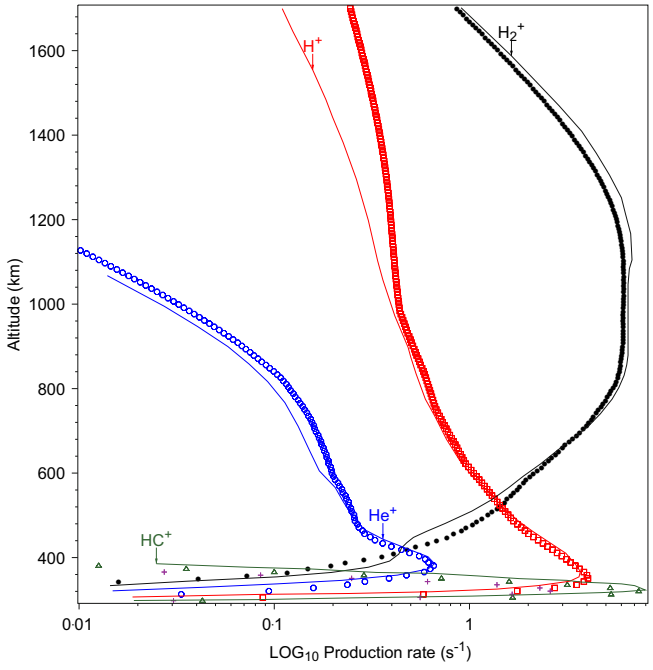

Fig. 4. Comparison of photoion production rates of Kim et al. [9] (labelled curves) for H_2^+, H^+, He^+ and hydrocarbon ions (HC^+) with those calculated in the current implementation: H_2^+ (•), H^+ (□), He^+ (○) and hydrocarbon ions (△).

these, 97 appropriate reactions from the Kinetic DataBase for Astrochemistry (KIDA) [10], as listed in Table 3, were substituted. The reaction rates for the hydrocarbons from the KIDA database are given there for temperature ranges of 10–280 K and 10–800 K. As the temperature range in the hydrocarbon layer at 300–380 km is 175–330 K [1] the rates for 10–280 K were used here.

2.4 Results and discussion

For the combined model the transitions between oxygen-containing species are shown in Figure 5. By comparison with Figure 1 it can be seen that the addition of photoionisation produces many more reactions and species.

In Figure 6 the densities of H_2O, CO and CO_2 predicted by the combined model (small symbols) are added to those for the meteoroid-only case (large symbols) previously shown in Figure 2. Also added are the densities of OH for the meteoroid-only case (△) and the combined case (△).

There are generally no discernible differences between the mixing ratios of H_2O, CO and CO_2 when photoionisation is included in the calculations. Hence the inclusion of photoionisation does not account for the overestimation of water density relative to the measurement at 100 km. However, there is a significant difference in the OH densities, with much higher values resulting from ionisation at altitudes above 400 km. The shape of this enhanced OH altitude profile is also different to that predicted for ionisation of the water emitted from the meteoroids [3]. Thus emissions from OH, produced by excitation of OH by photoelectrons, may provide a means of remote sensing of the processes by which water is added to Jupiter's atmosphere.

Dust could affect the calculation by attenuating the incoming solar flux or by becoming charged by photoelectron emission or electron attachment. One possible source of dust particles is meteoroids that do not completely ablate. However, Moses and Poppe [2] state that the incoming velocities on Jupiter are such that all of the grains completely ablate. This is consistent with the calculations of Rogers et al. [24] showing that meteoroids ablate completely if their speeds exceed 40 km s^{-1}. As the meteoroids at Jupiter have speeds in the range 60–70 km s^{-1} [2] complete ablation is therefore predicted. Another possible source of dust is the condensation of metallic species (Fe, Mg and Na) from silicate meteoroids onto aerosol particles. Kim et al. [9] predicted only very small densities of metallic ions above 600 km, thus such condensation is not expected to be significant at 800 km, where the major photoionization effect on OH density is predicted (see Fig. 6). While the presence of dust could remove ions and electrons in the altitude range 100–400 km [9] and so reduce the electron densities, this would not impact on the conclusion that inclusion of photoionisation does not result in a reduction in water densities at these altitudes.

Another source of oxygen input to Jupiter's atmosphere is SO_2 emitted from the moon Io. This is transferred via a plasma torus to Jupiter by ion precipitation in the auroral regions of Jupiter, where it could possibly then spread globally and contribute to chemistry in the non-auroral regions modeled here. However, Cravens and Eisenhower [25] calculated an auroral oxygen flux of 10^7 cm^{-2} s^{-1}, about equal to the meteoric flux [2] but over a much smaller area, and so not significant globally. SO_2^+ amounts to only 0.7% of the ions in the Io plasma torus, but elemental sulphur ions constitute about the same proportion (up to 30%) as oxygen ions [26]. Thus sulphur from Io may contribute to the chemistry of the non-auroral regions, but to simulate this would require

Table 3. Extra chemical reactions from KIDA [10] as utilised in this investigation. T is the temperature in K. These constants were typically defined for the range 10–280 K.

Reaction	Rate constant ($cm^3\ s^{-1}$)
$C_3H^+ + e^- \rightarrow C + CCH$	$1.08 \times 10^{-7}\ (T/300.)^{-0.5}$
$C_3H^+ + e^- \rightarrow H + C_3$	$1.83 \times 10^{-7}\ (T/300.)^{-0.5}$
$C_3H^+ + e^- \rightarrow C_2 + CH$	$9.00 \times 10^{-9}\ (T/300.)^{-0.5}$
$C_3H_2^+ + e^- \rightarrow C_2 + {}^1CH_2$	$1.26 \times 10^{-8}\ (T/300.)^{-0.5}$
$C_3H_2^+ + e^- \rightarrow H + H + C_3$	$5.46 \times 10^{-8}\ (T/300.)^{-0.5}$
$C_3H_2^+ + e^- \rightarrow H_2 + C_3$	$7.56 \times 10^{-8}\ (T/300.)^{-0.5}$
$C_3H_2^+ + e^- \rightarrow C + C_2H_2$	$1.13 \times 10^{-7}\ (T/300.)^{-0.5}$
$C_3H_2^+ + e^- \rightarrow H + C_3H$	$1.43 \times 10^{-7}\ (T/300.)^{-0.5}$
$C_3H_2^+ + e^- \rightarrow CH + CCH$	$2.10 \times 10^{-8}\ (T/300.)^{-0.5}$
$C_3H_3^+ + e^- \rightarrow CH + C_2H_2$	$6.0 \times 10^{-8}\ (T/300.)^{-0.5}$
$C_3H_3^+ + e^- \rightarrow H_2 + C_3H$	$0.5 \times 10^{-7}\ (T/300.)^{-0.5}$
$C_3H_3^+ + e^- \rightarrow H + C_3H_2$	$2.0 \times 10^{-7}\ (T/300.)^{-0.5}$
$C_3H_3^+ + e^- \rightarrow H + H_2 + C_3$	$0.5 \times 10^{-8}\ (T/300.)^{-0.5}$
$C_3H_5^+ + e^- \rightarrow H_2 + CH_2CCH$	$4.2 \times 10^{-8}\ (T/300.)^{-0.7}$
$C_3H_5^+ + e^- \rightarrow H + CH_3CCH$	$7.0 \times 10^{-8}\ (T/300.)^{-0.7}$
$C_3H_5^+ + e^- \rightarrow H + CH_2CCH_2$	$7.0 \times 10^{-8}\ (T/300.)^{-0.7}$
$C_3H_5^+ + e^- \rightarrow H + H + CH_2CCH$	$1.1 \times 10^{-7}\ (T/300.)^{-0.7}$
$C_3H_5^+ + e^- \rightarrow H + H_2 + C_3H_2$	$2.0 \times 10^{-7}\ (T/300.)^{-0.7}$
$C_3H_5^+ + e^- \rightarrow C_2H_2 + CH_3$	$4.7 \times 10^{-8}\ (T/300.)^{-0.7}$
$C_3H_5^+ + e^- \rightarrow H + {}^1CH_2 + C_2H_2$	$4.7 \times 10^{-8}\ (T/300.)^{-0.7}$
$C_3H_7^+ + e^- \rightarrow H + H + C_3H_5$	$8.80 \times 10^{-8}\ (T/300.)^{-0.7}$
$C_3H_7^+ + e^- \rightarrow H + H_2 + CH_3CCH$	$3.60 \times 10^{-8}\ (T/300.)^{-0.7}$
$C_3H_7^+ + e^- \rightarrow H + H_2 + CH_2CCH_2$	$3.60 \times 10^{-8}\ (T/300.)^{-0.7}$
$C_3H_7^+ + e^- \rightarrow H + CH_3 + C_2H_3$	$1.52 \times 10^{-7}\ (T/300.)^{-0.7}$
$C_3H_7^+ + e^- \rightarrow CH_3 + C_2H_4$	$3.20 \times 10^{-8}\ (T/300.)^{-0.7}$
$C_3H_7^+ + e^- \rightarrow H_2 + C_2H_2 + CH_3$	$8.80 \times 10^{-8}\ (T/300.)^{-0.7}$
$C_4H^+ + e^- \rightarrow C_2 + CCH$	$6.60 \times 10^{-8}\ (T/300.)^{-0.5}$
$C_4H^+ + e^- \rightarrow C + C_3H$	$8.50 \times 10^{-8}\ (T/300.)^{-0.5}$
$C_4H^+ + e^- \rightarrow H + C_4$	$5.70 \times 10^{-8}\ (T/300.)^{-0.5}$
$C_4H^+ + e^- \rightarrow H + C_3$	$1.20 \times 10^{-7}\ (T/300.)^{-0.5}$
$C_3H_4^+ + e^- \rightarrow H + CH_2CCH$	$3.00 \times 10^{-7}\ (T/300.)^{-0.7}$
$C_3H_4^+ + e^- \rightarrow {}^1CH_2 + C_2H_2$	$4.00 \times 10^{-8}\ (T/300.)^{-0.7}$
$C_3H_4^+ + e^- \rightarrow CCH + CH_3$	$3.00 \times 10^{-7}\ (T/300.)^{-0.7}$
$C_3H_4^+ + e^- \rightarrow H + H + C_3H_2$	$1.00 \times 10^{-7}\ (T/300.)^{-0.7}$
$C_4H_2^+ + e^- \rightarrow H_2 + C_4$	$1.50 \times 10^{-7}\ (T/300.)^{-0.5}$
$C_4H_2^+ + e^- \rightarrow H + C_4H$	$8.30 \times 10^{-7}\ (T/300.)^{-0.79}$
$C_4H_2^+ + e^- \rightarrow CH + C_3H$	$1.00 \times 10^{-8}\ (T/300.)^{-0.5}$
$C_4H_2^+ + e^- \rightarrow CCH + CCH$	$2.80 \times 10^{-7}\ (T/300.)^{-0.79}$
$C_4H_3^+ + e^- \rightarrow H_2 + C_4H$	$1.50 \times 10^{-7}\ (T/300.)^{-0.5}$
$C_4H_3^+ + e^- \rightarrow H + C_4H_2$	$4.10 \times 10^{-7}\ (T/300.)^{-0.7}$
$C_4H_3^+ + e^- \rightarrow CCH + C_2H_2$	$1.10 \times 10^{-7}\ (T/300.)^{-0.7}$
$C_4H_3^+ + e^- \rightarrow H + H + C_4H$	$6.20 \times 10^{-8}\ (T/300.)^{-0.7}$
$C_4H_3^+ + e^- \rightarrow {}^3CH_2 + C_3H$	$3.70 \times 10^{-8}\ (T/300.)^{-0.7}$
$C_4H_5^+ + e^- \rightarrow H_2 + H_2 + C_4H$	$1.01 \times 10^{-7}\ (T/300.)^{-0.5}$
$C_4H_5^+ + e^- \rightarrow H + H_2 + C_4H_2$	$1.01 \times 10^{-7}\ (T/300.)^{-0.5}$
$C_4H_5^+ + e^- \rightarrow C_2H_2 + C_2H_3$	$1.01 \times 10^{-7}\ (T/300.)^{-0.5}$
$C_4H_5^+ + e^- \rightarrow CCH + C_2H_4$	$1.01 \times 10^{-7}\ (T/300.)^{-0.5}$
$C_4H_5^+ + e^- \rightarrow CH + CH_3CCH$	$4.50 \times 10^{-8}\ (T/300.)^{-0.5}$
$C_4H_7^+ + e^- \rightarrow H_2 + H_2 + H_2 + C_4H$	$6.00 \times 10^{-8}\ (T/300.)^{-0.5}$
$C_4H_7^+ + e^- \rightarrow CH_4 + CH_2CCH$	$1.95 \times 10^{-7}\ (T/300.)^{-0.5}$
$C_4H_7^+ + e^- \rightarrow C_2H_3 + C_2H_4$	$2.25 \times 10^{-8}\ (T/300.)^{-0.5}$
$C_4H_7^+ + e^- \rightarrow C_2H_2 + C_2H_5$	$2.25 \times 10^{-8}\ (T/300.)^{-0.5}$
$C_3H_9^+ + e^- \rightarrow H + C_3H_8$	$2.00 \times 10^{-7}\ (T/300.)^{-0.7}$
$C_3H_9^+ + e^- \rightarrow H + H + C_3H_7$	$2.00 \times 10^{-7}\ (T/300.)^{-0.7}$
$C_3H_9^+ + e^- \rightarrow CH_3 + C_2H_6$	$1.00 \times 10^{-7}\ (T/300.)^{-0.7}$
$C_3H_9^+ + e^- \rightarrow H_2 + CH_3 + C_2H_4$	$1.00 \times 10^{-7}\ (T/300.)^{-0.7}$
$C_2H_5O^+ + e^- \rightarrow CH_3 + H_2CO$	$1.5 \times 10^{-7}\ (T/300.)^{-0.5}$
$C_2H_5O^+ + e^- \rightarrow H + H_2 + H_2CCO$	$1.5 \times 10^{-7}\ (T/300.)^{-0.5}$
$C_2H_5O^+ + e^- \rightarrow H + CO + CH_4$	$3.0 \times 10^{-7}\ (T/300.)^{-0.5}$
$C_2H_5O^+ + e^- \rightarrow H + CH_3CHO$	$1.5 \times 10^{-7}\ (T/300.)^{-0.5}$
$C_2H_7O^+ + e^- \rightarrow H + H_2O + C_2H_4$	$1.5 \times 10^{-7}\ (T/300.)^{-0.5}$
$C_2H_7O^+ + e^- \rightarrow H + H_2 + CH_3CHO$	$1.5 \times 10^{-7}\ (T/300.)^{-0.5}$
$C_2H_7O^+ + e^- \rightarrow H + CH_3CH_2OH$	$1.5 \times 10^{-7}\ (T/300.)^{-0.5}$
$HCO^+ + e^- \rightarrow H + CO$	$2.80 \times 10^{-7}\ (T/300.)^{-0.69}$
$OCH^+ + e^- \rightarrow H + CO$	$2.80 \times 10^{-7}\ (T/300.)^{-0.69}$
$OCH_3^+ + e^- \rightarrow H + CO + H_2$	$2.00 \times 10^{-7}\ (T/300.)^{-0.5}$
$OCH_3^+ + e^- \rightarrow H + H + HCO$	$2.00 \times 10^{-7}\ (T/300.)^{-0.5}$
$OCH_3^+ + e^- \rightarrow H + H_2CO$	$2.00 \times 10^{-7}\ (T/300.)^{-0.5}$
$O + C_3H_2^+ \rightarrow CCH + HCO^+$	4.0×10^{-10}
$O + C_3H_3^+ \rightarrow CO + C_2H_3^+$	$1.00 \times 10^{-9}\ e^{-2600/T}$
$O + C_3H_3^+ \rightarrow CO + C_2H_3^+$	4.50×10^{-11}
$O + C_3H_3^+ \rightarrow HCO + C_2H_2^+$	3.80×10^{-11}
$O + C_3H_3^+ \rightarrow H_2 + HC_3O^+$	2.30×10^{-11}
$O + C_3H_3^+ \rightarrow H_2 + H_2C_3O^+$	4.5×10^{-11}
$O + C_3H_5^+ \rightarrow C_2H_4 + HCO^+$	2.00×10^{-10}
$O + C_4H^+ \rightarrow C_3 + HCO^+$	2.0×10^{-10}
$O + C_3H_4^+ \rightarrow CH_3 + HCO^+$	2.0×10^{-10}
$O + C_4H_2^+ \rightarrow H + HC_4O^+$	1.35×10^{-10}
$O + C_4H_2^+ \rightarrow CO + C_3H_2^+$	1.10×10^{-10}
$O + C_4H_3^+ \rightarrow C_3H_2 + HCO^+$	2.00×10^{-13}
$C_3H_6^+ + e^- \rightarrow H + H_2 + C_3H_3$	$3.5 \times 10^{-7}\ (300./T)^{0.5}$
$C_3H_8^+ + e^- \rightarrow H + H + C_3H_6$	$3.5 \times 10^{-7}\ (300./T)^{0.5}$
$C_4H_9^+ + e^- \rightarrow C_2H_4 + C_2H_5$	$3.5 \times 10^{-7}\ (300./T)^{0.5}$
$OC_2H^+ + e^- \rightarrow C + H + CO$	$1.1 \times 10^{-7}\ (300./T)$
$HOC^+ + e^- \rightarrow H + CO$	$2.00 \times 10^{-7}\ (T/300.)^{-0.75}$
$CH_3OH_2^+ + e^- \rightarrow H + H_2 + H_2CO$	$9.10 \times 10^{-8}\ (T/300.)^{-0.670}$
$CH_3OH_2^+ + e^- \rightarrow H_2O + CH_3$	$8.19 \times 10^{-8}\ (T/300.)^{-0.670}$
$CH_3OH_2^+ + e^- \rightarrow H + OH + CH_3$	$4.64 \times 10^{-7}\ (T/300.)^{-0.670}$
$CH_3OH_2^+ + e^- \rightarrow H + {}^3CH_2 + H_2O$	$1.91 \times 10^{-7}\ (T/300.)^{-0.670}$
$CH_3OH_2^+ + e^- \rightarrow H + CH_3OH$	$2.73 \times 10^{-8}\ (T/300.)^{-0.670}$
$CCH + H \rightarrow C_2 + H_2$	$5.99 \times 10^{-11} e^{-14200/T}$
$CH_2CCH + H_2 \rightarrow H + CH_3CCH$	$1.42 \times 10^{-13}\ (T/300.)^{2.38} e^{-9560/T}$
$CH_3CCH + H \rightarrow H_2 + CH_2CCH$	$4.50 \times 10^{-12}\ (T/300.)^{2.00} e^{-2520/T}$
$C_4 + H_2 \rightarrow H + C_4H$	$1.60 \times 10^{-10} e^{-1420/T}$
$CH_3CH_2OH + He^+ \rightarrow H + He + H_2CO + CH_3^+$	$1.32 \times 10^{-9}\ (T/300.)^{-0.5}$
$HC_3O^+ + e^- \rightarrow O + C_3H$	$3.00 \times 10^{-7}\ (T/300.)^{-0.5}$
$HC_3O^+ + e^- \rightarrow H + C_3O$	$1.50 \times 10^{-7}\ (T/300.)^{-0.5}$
$HC_3O^+ + e^- \rightarrow CO + CCH$	$2.50 \times 10^{-7}\ (T/300.)^{-0.5}$
$H_2C_3O^+ + e^- \rightarrow CO + C_2H_2$	$1.50 \times 10^{-7}\ (T/300.)^{-0.7}$
$H_2C_3O^+ + e^- \rightarrow OH + C_3H$	$3.00 \times 10^{-7}\ (T/300.)^{-0.5}$
$H_2C_3O^+ + e^- \rightarrow H + H + C_3O$	$7.00 \times 10^{-8}\ (T/300.)^{-0.7}$
$H_2C_3O^+ + e^- \rightarrow H + HC_3O$	$0.55 \times 10^{-7}\ (T/300.)^{-0.7}$
$H_2C_3O^+ + e^- \rightarrow H + CO + CCH$	$3.50 \times 10^{-7}\ (T/300.)^{-0.7}$
$HC_4O^+ + e^- \rightarrow CO + C_3H$	$3.00 \times 10^{-7}\ (T/300.)^{-0.5}$
$HC_4O^+ + e^- \rightarrow CH + C_3O$	$1.50 \times 10^{-7}\ (T/300.)^{-0.5}$
$C + C_3O \rightarrow CO + C_3$	1.00×10^{-10}
$H + HC_3O \rightarrow CO + C_2H_2$	2.00×10^{-10}

three-dimensional modeling of the auroral processes and horizontal transport.

In the simulations the electron temperature T_e was assumed to be the same as the neutral temperature T. In reality the photoelectrons have a higher mean energy when initially produced, which is lost in collisions producing further ionisation (including more H_2^+) and excitation of atoms and molecules. This gives $T_e > T$ and thus lower recombination rates. As there are no competing electron-loss processes at higher altitudes, the electrons must still recombine and so the only difference due to a different T_e would be a different mix of recombination reaction rates. This was investigated by running the simulation with $T_e = 2T$, with the finding that there was no significant change to the predicted OH densities.

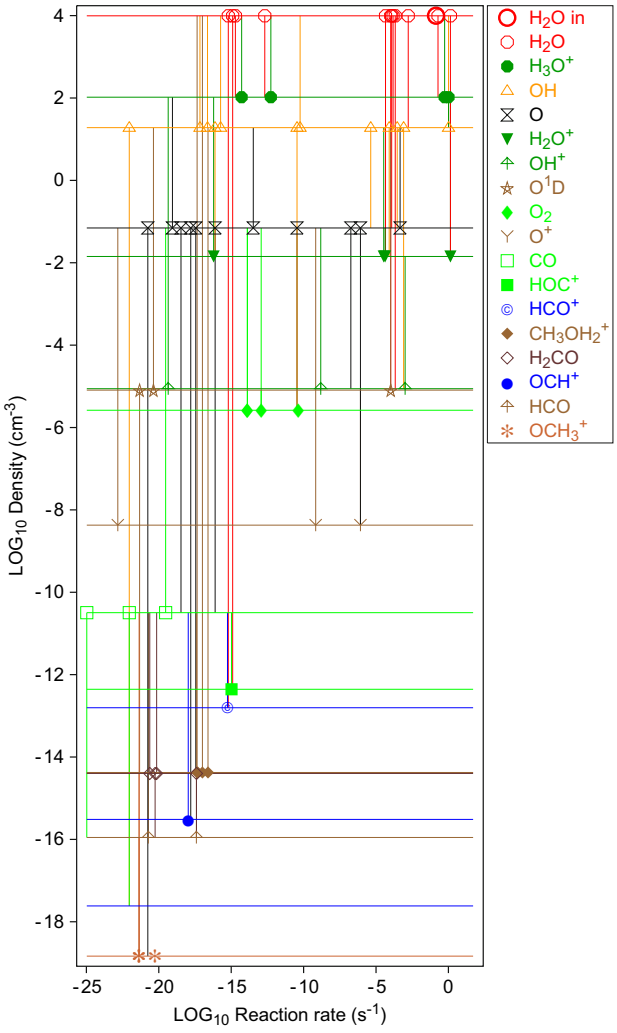

Fig. 5. Transitions between oxygen-containing species for the case including photoionisation at 629 km, represented by lines joining reactants and products plotted at the reaction rate (s^{-1}) on the horizontal axis, with the densities of the species shown on the vertical axis. Reactants are identified by symbols described in the legend. The meteoric input rate of H_2O ("H_2O in") is shown by a larger circle.

Electron–neutral processes were not considered, as negative ions are not considered in either the model of Kim et al. [9] or in other models of Jupiter's upper atmosphere by Majeed and McConnell [27] and Yelle and Miller [28]. However, as negative ions were observed to have unexpectedly large densities in the atmosphere of Titan [29], (which also has methane as a constituent), electron–neutral processes should be considered in more comprehensive modelling.

3 Conclusions

Building on a previous model that considered photochemistry and meteoric input in a simulation of the composition of the atmosphere of Jupiter, photoionisation has been added. While this change did not alter the calculated water densities and thus explain the overestimation of these relative to an available measurement, the calculated densities of OH were significantly changed. Thus electron-driven emissions from OH may be useful as a means of remote sensing of the processes by which oxygen is added to the atmosphere of Jupiter.

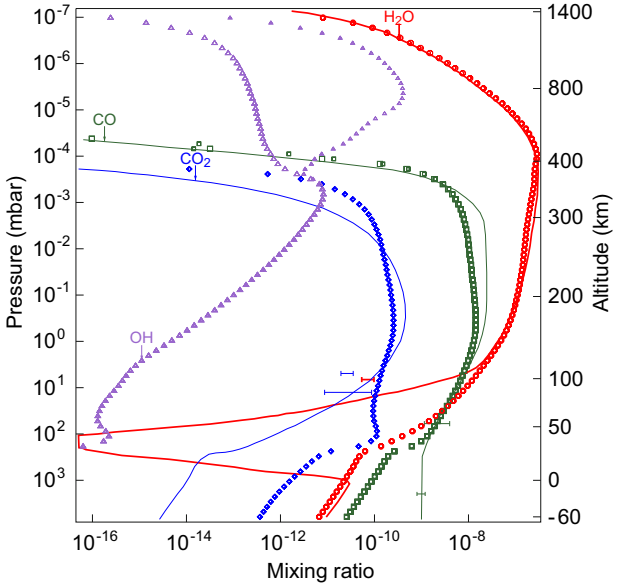

Fig. 6. Mixing ratios (horizontal axis) of H_2O, CO, CO_2 and OH as a function of pressure (mbar)/altitude (km). Values calculated by Moses and Poppe [2] are shown by labelled curves. Error bars show measured values. Mixing ratios determined in the current implementation of that model are shown by large symbols: H_2O (○), CO (□), CO_2 (◇) and OH (△) and for the combined model by smaller symbols: H_2O (○), CO (□), CO_2 (◇) and OH (△).

We thank the Australian Research Council for support of the development of this modelling through grant DP160102787 and grant DP180101655.

Author contribution statement

LC did the computational modelling for this paper, under the scientific direction of MJB and checking by DBJ. RDW gave advice on the development of the computational model, while GG, OI and MCAL helped with background information on photoionisation processes, low-energy electron interactions and ionisation of methane. All authors contributed to the writing and editing of this paper, both in its original form and on revision due to helpful comments from the referees.

References

1. J.I. Moses, T. Fouchet, B. Bézard, G.R. Gladstone, E. Lellouch, H. Feuchtgruber, J. Geophys. Res. **110**, E08001 (2005)

2. J.I. Moses, A.R. Poppe, Icarus **297**, 33 (2017)
3. L. Campbell, M.J. Brunger, Icarus **326**, 162 (2019)
4. L. Campbell, M.J. Brunger, Int. Rev. Phys. Chem. **35**, 297 (2016)
5. R. Riahi, Ph. Teulet, Z. Ben Lakhdar, A. Gleizes, Eur. Phys. J. D **40**, 223 (2006)
6. L. Campbell, M.J. Brunger, Planet Space Sci. **151**, 11 (2018)
7. V.L.K. Chakrabarti, J. Tennyson, Plasma Sources Sci. Technol. **28**, 085013 (2019)
8. Y.H. Kim, J.L. Fox, Icarus **112**, 310 (1994)
9. Y.H. Kim, W. Dean Pesnell, J.M. Grebowsky, J.L. Fox, Icarus **150**, 161 (2001)
10. Kinetic Database for Astrochemistry (KIDA), accessed 13 September 2019, http://kida.obs.u-bordeaux1.fr/
11. G.R. Gladstone, M. Allen, Y.L. Yung, Icarus **119**, 1 (1996)
12. M.R. Torr, D.G. Torr, R.A. Ong, H.E. Hingeregger, Geophys. Res. Lett. **6**, 771 (1979)
13. S.C. Solomon, L. Qian, J. Geophys. Res. **110**, A10306 (2005)
14. Community Coordinated Modeling Center (CCMC), Accessed 6 June 2019, https://ccmc.gsfc.nasa.gov/pub/modelweb/solar/euv/ae-euv
15. H.E. Hinteregger, K. Fukui, B.R. Gilson, Geophys. Res. Lett. **8**, 1147 (1981)
16. NIFS data base, Accessed 14 November 2014, http://dpc.nifs.ac.jp/photoab/atom/H/DBASE_H_table.txt
17. J.A.R. Samson, G.N. Haddad, J. Opt. Soc. Am. B **11**, 277 (1994)
18. K. Kirby, E.R. Constantinides, S. Babeu, M. Oppenheimer, G.A. Victor, At. Data Nucl. Data Tables **23**, 63 (1979)
19. J.A.R. Samson, G.N. Haddad, T. Masuoka, P.N. Pareek, D.A.L. Kilcoyne, J. Chem. Phys. **90**, 6925 (1989)
20. J.A.R. Samson, Adv. At. Mol. Phys. **2**, 177 (1996)
21. T. Hayaishi, S. Iwata, M. Sasanuma, E. Ishiguro, Y. Morioka, Y. Iida, M. Nakamura, J. Phys. B: At. Mol. Phys. **15**, 79 (1982)
22. H. Kossman, O. Schwarzkopf, B. Kämmerling, W. Braun, V. Schmidt, J. Phys. B: At. Mol. Opt. Phys. **22**, L411 (1989)
23. C. Backx, G.R. Wright, M.H. Van der Wiel, J. Phys. B: At. Mol. Phys. **9**, 315 (1976)
24. L.A. Rogers, K.A. Hill, R.L. Hawkes, Planet. Space Sci. **53**, 1341 (2005)
25. T.E. Cravens, G.M. Eisenhower, Icarus **100**, 260 (1992)
26. K.M. Bodisch, L.P. Dougherty, F. Bagenal, J. Geophys. Res. Space Phys. **122**, 8277 (2017)
27. T. Majeed, J.C. McConnell, Planet. Space Sci. **39**, 1715 (1991)
28. R.V. Yelle, S. Miller, in *Jupiter's Thermosphere and Ionosphere* (Cambridge University Press, 2004), p. 185
29. A.J. Coates, F.J. Crary, G.R. Lewis, D.T. Young, J.H. Waite Jr., E.C. Sittler Jr., Geophys. Res. Lett. **34**, L22103 (2007)